

High performance perovskite sub-module with sputtered SnO₂ electron transport layer

Guangfeng Bai^a, Zhengli Wu^a, Jing Li^a, Tongle Bu^a, Wangnan Li^b, Wei Li^a, Fuzhi Huang^a, Qi Zhang^{c,d}, Yi-Bing Cheng^{a,e}, Jie Zhong^{a,e}

^a State Key Laboratory of Advanced Technology for Materials Synthesis and Processing, Wuhan University of Technology, Wuhan 430070, China

^b Hubei Key Laboratory of Low Dimensional Optoelectronic Materials and Devices, Hubei University of Arts and Science, Xiangyang 441053, China

^c School of Aerospace, Transport and Manufacturing, Cranfield University, Cranfield, Bedfordshire MK43 0AL, UK

^d School of Materials Science and Engineering, Wuhan University of Technology, Wuhan 430070, China

^e Department of Materials Science and Engineering, Monash University, VIC 3800, Australia

ARTICLE INFO

Keywords:

Magnetron sputter
Tin oxide
Perovskite solar cell
Module
High efficiency

ABSTRACT

Hybrid perovskite solar cells (PSC) have gained stupendous achievement in single/tandem solar cell, semi-transparent solar cell and flexible devices. Aiming for potential commercialization of perovskite photovoltaic technology, up scalable processing is crucial for all function layers in PSC. Herein we present a study on room temperature magnetron sputtering of tin oxide electron transporting layer (ETL) and apply it in a large area PSC for low cost and continues manufacturing. The SnO₂ sputtering targets with varied oxygen and deposition models are used. Specifically, the working gas ratio of Ar/O₂ during the radio frequency sputtering process plays a crucial role to obtain optimized SnO₂ film. The sputtered SnO₂ films demonstrate similar morphological and crystalline properties, but significant varied defect states and carrier transportation roles in the PSC devices. With further modification of thickness of SnO₂, the PSCs based on sputtered SnO₂ ETL shows a champion efficiency of 18.20% in small area and an efficiency of 14.71% in sub-module with an aperture area of 16.07 cm², which is the highest efficiency of perovskite sub module with sputtered ETLs.

1. Introduction

Hybrid perovskite solar cells (PSCs) have attracted stupendous attention due to their low-cost solution printability (Bu et al., 2018) and remarkable power conversion efficiency (PCE). Up to date, various efforts have been contributed to improve the performance of PSCs, and a certified PCE based on a small area cell (< 0.1 cm²) has exceeded 23% recently, which makes it promising to compete with silicon solar cells (Jeon et al., 2018). There is also exclusive superiority for PSC in tandem solar cells (Leijtens et al., 2018; Zhao et al., 2018a; Albrecht et al., 2016; Bush et al., 2018), semitransparent solar cells (Xue et al., 2018; Zhang et al., 2018; Xie et al., 2018), and flexible devices (Feng et al., 2018; Bu et al., 2018). However, the instability of perovskite absorber materials (Correa-Baena et al., 2017) and difficulty in large area fabrication devices (Li et al., 2018b) is still serious problems for future commercialization of perovskite-based solar cell.

So far, the planar n-i-p structured PSCs (Halvani Anaraki et al., 2018; Yang et al., 2018a) shows great promise due to their easier up-scaling deposition of electron transport layers (ETLs) compared to

mesostructured PSCs (Petrović et al., 2017). And there are lots of fabrication methods (Chen et al., 2019) have been reported to efficiently deposit thin ETL films, however, not all the methods are suitable for achieving uniform large area high quality thin films for large area perovskite solar modules (PSMs). For example, solution based preparation methods such as spin-coating (Yang et al., 2018b) and chemical bath deposition (Anaraki et al., 2016) suffer from necessary annealing process, and the quality of the sintered films are sensitive to the external environmental conditions including humidity (Li et al., 2018a; Bu et al., 2016), oxygen and, etc., which results in poor reproducibility and is fatal to industrial production. Another widely reported method of atomic layer deposition (Wang et al., 2016; Correa Baena et al., 2015) (ALD) to fabricate ETLs for PSCs exhibits excellent stability and reproducibility, which can be attributed to the homogeneity of monolayer deposition. However, the high cost of precursor solutions is not suitable for pursuing economical large-scale application. Vacuum fabrication (Ma et al., 2017; Chen et al., 2017), especially for magnetron sputtering (Qiu et al., 2018), owns considerable superiority compare to aforementioned preparation methods due to its sophisticated applications. It

is convenient to produce all sorts of large area uniform thin films (semiconductor (Aydin et al., 2018; Guo et al., 2018; Silva Filho et al., 2018) and alloy (Huang et al., 2015)) in industry and effective to control the morphology and crystallinity of film via sputter process, and which could be perfectly applied in thin ETL films preparation for large size PSMs.

To date, several inorganic semiconductor materials (Chen et al., 2019) have been applied in the PSCs as ETL by sputtering such as TiO₂, SnO₂ and ZnO (Kogo et al., 2018; Zhao et al., 2018b; Qiu et al., 2018). Jin et al. achieved a current density of 24.19 mA/cm² for PSCs by direct current (DC) magnetron sputtering through modulating the dominated plane facet of TiO₂, which contributes a high efficiency of 17.25% (Huang et al., 2017). Although low electron mobility and surface defect of TiO₂ can be resolved by doping (Roose et al., 2016) and modification (Lee et al., 2015), the cost of process are increased as well, besides, the TiO₂ may decrease the stability of perovskite due to the poor UV-resistance (Guo et al., 2015). Liu et al. used the radio frequency (RF) magnetron sputtered ZnO films to fabricate planar PSCs, and which obtained a best efficiency of 16.60% by adjusting Ar/O₂ gas ratio (Zhao et al., 2018b). However, the possible reaction between ZnO and per-ovskite may cause instability to PSCs (Yin et al., 2016). Comparing with TiO₂ and ZnO, the SnO₂ possesses numerous merits such as high mobility and well matching with perovskite energy level (Correa Baena et al., 2015; Jiang et al., 2016), especially can be prepared in room-temperature, which is a promising for low-cost and environmental friendly fabrication of large size PSMs. Very few reports were presented on sputtered SnO₂ ETL in planar PSC show relative low performance for the PSCs (Tao et al., 2018; Ali et al., 2018). Fang et al. obtained a small area efficiency of 13.68% for planar PSC with sputtered SnO₂ prepared at room temperature (Tao et al., 2018). The advantage of sputtering SnO₂ in large area has been demonstrated until recently by Qi et al. and achieved an efficiency over 12% for perovskite sub-modules (Qiu et al., 2018). However, this result is still much lower than solution processed SnO₂ PSMs (Bu et al., 2017). To further improving the performances of large area PSMs with sputter SnO₂ ETL, investigation aiming for uniform deposition and insight understanding of the reaction process of sputtering is required.

Herein, we fabricated highly efficient and large-area planar perovskite solar cells based on sputtered SnO₂ ETLs at room temperature with significantly enhanced sub-module efficiency. Two types of SnO₂ targets sputtered by RF and DC supplies were investigated and found that the devices based on SnO₂ ETL which is sputtered by RF shows preferable performance. We systematic explored the effects of oxygen vacancy in structural, morphological and electrical properties of SnO₂ films by adjusting the flow rate of Ar/O₂ gas in the sputtering process. The working gas ratio of Ar/O₂ during the sputtering process plays a crucial role in obtain optimized SnO₂ film and the efficiency of PSCs. With further optimizing of the film thickness, post-annealing temperature of sputtered SnO₂ ETLs, the as obtained PSCs obtained the champion PCEs of 18.20% in small area and 14.71% in sub-module (with an aperture area 16.07 cm²) respectively, as well as excellent reproducibility.

2. Experimental details

2.1. Materials

White SnO₂ target was purchased from Changsha Xinkang Advanced Material Corporation LTD and gray SnO₂ target was purchased from www.znxc.com.cn. Formamidinium iodide (FAI), methy-lammonium bromine (MABr) and Spiro-OMeTAD were purchased from Lumtec, Taiwan. Lead iodide (PbI₂) and lead bromine (PbBr₂) were purchased from Xi'an Polymer Light Technology Crop. CsI and KI were purchased from Sigma-Aldrich. Unless specific instructions, otherwise all chemicals were purchased from Sigma-Aldrich and used as received.

2.2. Preparation of SnO₂ films

The FTO substrate were etched by a femtosecond laser machine followed by ultrasonic cleaning method. All the substrate was treated by UV-ozone for 15 min before fixed on substrate holder in the chamber. The deposition process start (magnetron sputtering system, Angstrom Engineering Ltd) after the chamber was pump down below 8×10^{-4} Pa and the deposition pressure was kept at 1 mT with a turbo pump. The total flow rate of argon gas and oxygen gas was 30 sccm while the argon gas is used for plasma triggering. For better coverage, the sputter rate was adjusted to 0.1 Å/s. All films were deposited at room temperature. The thickness of film controlled by Quartz Monitor Crystals was calibrated by step profiler in the first time. After sputter process, the sample was taken out once and being transferred to N₂-filled glove box.

2.3. Device fabrication

The sputtered SnO₂ film was treated with UV-ozone for 20 min before the spin-coating of perovskite layer in N₂-filled glove box. The FA_{0.85}MA_{0.15}Pb(I_{0.85}Br_{0.15})₃ was prepared according to the literature (Liu et al., 2018). The perovskite solution was spin coated on the SnO₂/FTO substrate at 6000 rpm with an accelerated speed of 1000 rpm, which consists of 0.85 PbI₂ and 0.15 PbBr₂, and 1.3 M organic cation which are composed of 0.85 FAI and 0.15 MABr in the mixture solvent of DMF/DMSO (4:1, by volume). The KCsFAMA mixed perovskite precursor was prepared by add different amount of KI (predissolved as a 2 M stock solution in DMSO) and CsI (predissolved as a 2 M stock solution in DMSO) to FAMA mixed perovskite solution to achieve the desired K_xCsFAMA perovskite solution. During the last 5th second in the spin coating process, 90 μL anti-solvent of ethyl acetate (EA) was dropped slowly on the spinning substrate in order to form a smooth and no pinhole precursor film. The films were then annealed at 120 °C for 45 min. After cooling down to room temperature, a 25 μL Spiro-OMeTAD solution was spun on the mixed perovskite film at 3000 rpm for 30 s, which was prepared by dissolving 73 mg Spiro-OMeTAD into 1 mL chlorobenzene and doped by 18 μL Li-TFSI (pre-dissolved as a 520 mg/mL stock solution in acetonitrile) and 29 μL FK209 (pre-dissolved as a 300 mg/mL stock solution in acetonitrile) and 30 μL 4-*tert*-butylpyridine. Lastly, a 60 nm of gold was evaporated on the top of Spiro-OMeTAD layer as the back electrode to fulfil the complete devices.

The fabrication of sub-modules based on the previous reports (Bu et al., 2017) in our lab. Firstly, the FTO glass cut into 5 cm × 6 cm was etched by a femtosecond laser to separate the electrodes with six strips. Secondly, the cleaned substrate was deposited with SnO₂ film by RF magnetron sputtering system at room temperature. And then, the per-ovskite and Spiro-OMeTAD films were prepared by spin-coating, the same process as the small devices. Finally, the sample was etched again with the femtosecond laser to generate a series-connected module before depositing the gold electrode.

2.4. Characterizations

The morphologies and microstructures of the SnO₂ and perovskite films were both investigated using a field-emission scanning electron microscopy (FESEM, Zeiss Ultra Plus). The surface morphology and roughness of SnO₂ film were tested by atomic force microscope (AFM, SPM9700, Shimadzu, Japan). The crystallinity of sputtered SnO₂ films were characterized by an X-ray diffractometer (XRD, D8 Advance). The transmittance and absorbance spectra were measured with a UV-Vis spectrometer (lambda 750S, PerkinElmer). The composition and binding energy spectrum of sputtered SnO₂ film were characterized by X-ray photoelectron spectroscopy (XPS) and ultraviolet photoelectron spectroscopy (UPS) methods using a XPS/UPS system (Thermo Scientific, Escalate 250Xi). The EIS measurements were carried out by a

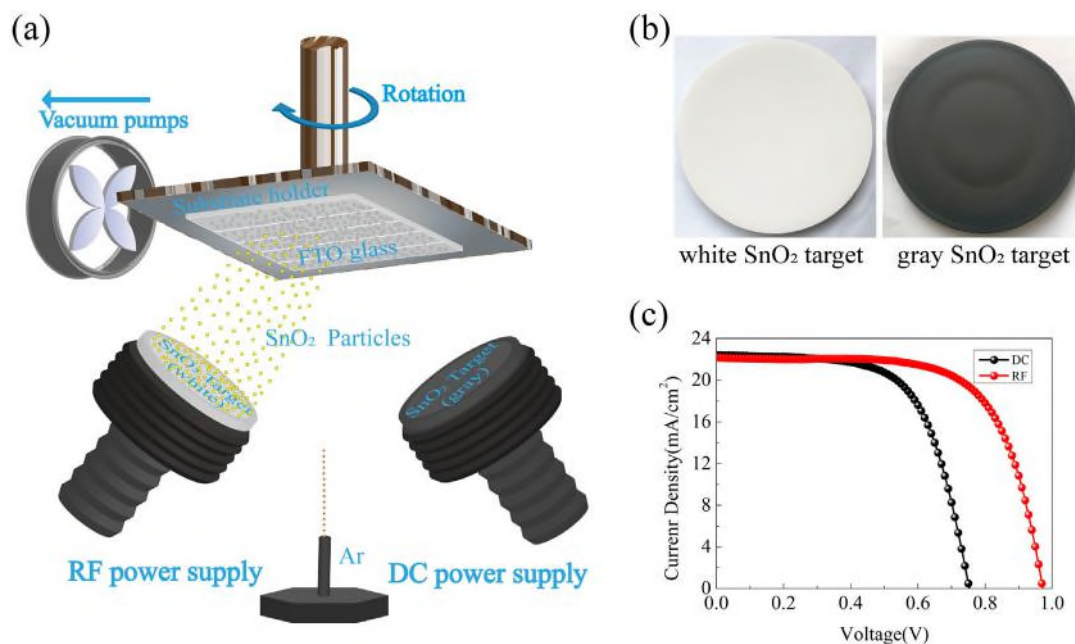


Fig. 1. (a) Schematic illustration of SnO₂ deposition process of DC/RF magnetron sputtering. (b) Two types of SnO₂ targets. (c) *J-V* curves of PSC based on DC/RF sputtered SnO₂ ETL.

EC-lab (SP300). The steady-state PL and time-resolved PL decay spectrum was measured by fluorescence spectrometer (FLS 980), with a 507 nm laser (EPL-510, Edinburgh Instruments Ltd). The *J-V* curves of the PSCs were measured using a solar simulator (Oriol 94023A, 300 W) and a Keithley 2400 source meter. The intensity (100 mW/cm²) was calibrated using a standard Si solar cell (Oriol, VLSI standards). All the devices were tested under AM 1.5G sun light (100 mW/cm²) using metal masks of 0.1475 cm² for the small PSCs and 16.07 cm² for the 5 cm × 6 cm PSC modules, respectively.

3. Results and discussion

That the schematic illustration of SnO₂ deposition process use RF/ DC magnetron sputtering is showed in Fig. 1a. The SnO₂ particles are sputtered by high energy argon ions, react with the reaction gas (high purity oxygen), and deposited on the top of the FTO. The rotatable substrate holder ensures the uniformity of SnO₂ film and the thickness can be precisely controlled by Quartz Monitor Crystals. The deposition process is continuous as long as the FTO substrates is replaced after one sputtering. High target material utilization ratio and room-temperature fabrication process further reduces production costs. Moreover, the preparation process is performed in a high vacuum chamber, which is beneficial to obtain high reproducibility without environmental contamination.

There are two types of SnO₂ targets as shown in Fig. 1b. The one that is sputtered by DC power is conductive gray SnO₂ target, which is prepared by hot pressed sintering under a reducing atmosphere. Another one that is sputtered by RF power is nonconductive white SnO₂ target, which is produced from high-purity SnO₂ powder under normal atmosphere. Fig. 1c shows the comparison of the device's performance between DC and RF sputtering under the same condition (Ar/O₂ = 4:1). The SnO₂ films by RF sputtering have a noticeable improvement in device efficiency than DC sputtering. The device based on SnO₂ ETL which is sputtered by RF shows superior voltage and FF. Hence, the detailed research was conducted in non-conducting white SnO₂ target by RF sputtering.

The SnO₂ film is deposited onto the surface of FTO glass by adjusting Ar/O₂ gas ratio and controlling thickness. At the beginning, the surface of white SnO₂ target which is sputtered in Ar-rich (Ar:O₂ > 2)

atmosphere becomes tan (Fig. S1), and thus leading to poor performance. While increasing the oxygen gas, the surface of target turns to light yellow or white. Therefore, we carefully investigate how the Ar/O₂ ratio will impact on the device performance in oxygen-rich atmosphere.

The X-ray photoelectron spectroscopy (XPS) is employed to characterize the electronic states and composition information of sputtered SnO₂ film. The full XPS spectra of sputtered SnO₂ with various Ar/O₂ ratio are shown in Fig. S2, showing the existence of Sn and O. Fig. 2a presents the Sn 3*d* core level spectra of sputtered SnO₂ films with different Ar/O₂ ratios. That only two peaks occur at the binding energy of about 486.7 eV and 495.2 eV are observed, corresponding to the Sn 3*d*_{5/2} and Sn 3*d*_{3/2}, respectively. The Sn 3*d* peaks displays one symmetric shape without any shoulder, which indicates only a Sn⁴⁺ chemical state. These results also reveal that the binding energy of Sn 3*d* can hardly be affected by Ar/O₂ ratios (O₂-rich condition). The O 1*s* XPS spectra of sputtered SnO₂ film with different Ar/O₂ ratios are shown in Fig. 2b, which displays slight asymmetry in its shape. The O 1*s* spectra of sputtered SnO₂ can be decomposed into two components corresponding to Sn⁴⁺-O (530.7 eV) and C-Ox (531.8 eV). The areas of Sn⁴⁺-O contribution of O 1*s* core level and Sn 3*d* core level was used to calculate the ratio of O: Sn. From Fig. 2c, with the decrease of Ar/O₂ ratio, the ratio of O/Sn increases gradually from 1.869 to 1.966. Table S1 shows the position and O/Sn ratio for the sputtered SnO₂ film under various Ar/O₂ ratio. Oxygen vacancy in ETL film plays a crucial role in fabricating high performance PSC (Zhang et al., 2016). By adjusting the ratio of Ar/O₂ during the sputtering process, the ratio of O/Sn in SnO₂ film can be controlled. The O/Sn ratio in SnO₂ film does not increase to stoichiometric ratio 2:1 although excessive oxygen reactive gas is introduced in the sputtering process, which indicates a certain quantity of oxygen vacancy in sputtered SnO₂ film.

The crystallinity of room-temperature sputtered SnO₂ film are investigated by X-ray diffraction (XRD), shown in Fig. 2d. The SnO₂ film are sputtered in room-temperature and without any post annealing. Owing to introduce oxygen gas in sputter process, the (1 0 1) and (2 1 1) lattice planes of SnO₂ are observed, and no other planes of SnO could be found, indicating that the sputtered films are pure SnO₂ (Jiang et al., 2016; Ma et al., 2017). Besides, as the increasing of oxygen ratio, the intensity of the diffraction peaks with (1 0 1) lattice plane of SnO₂

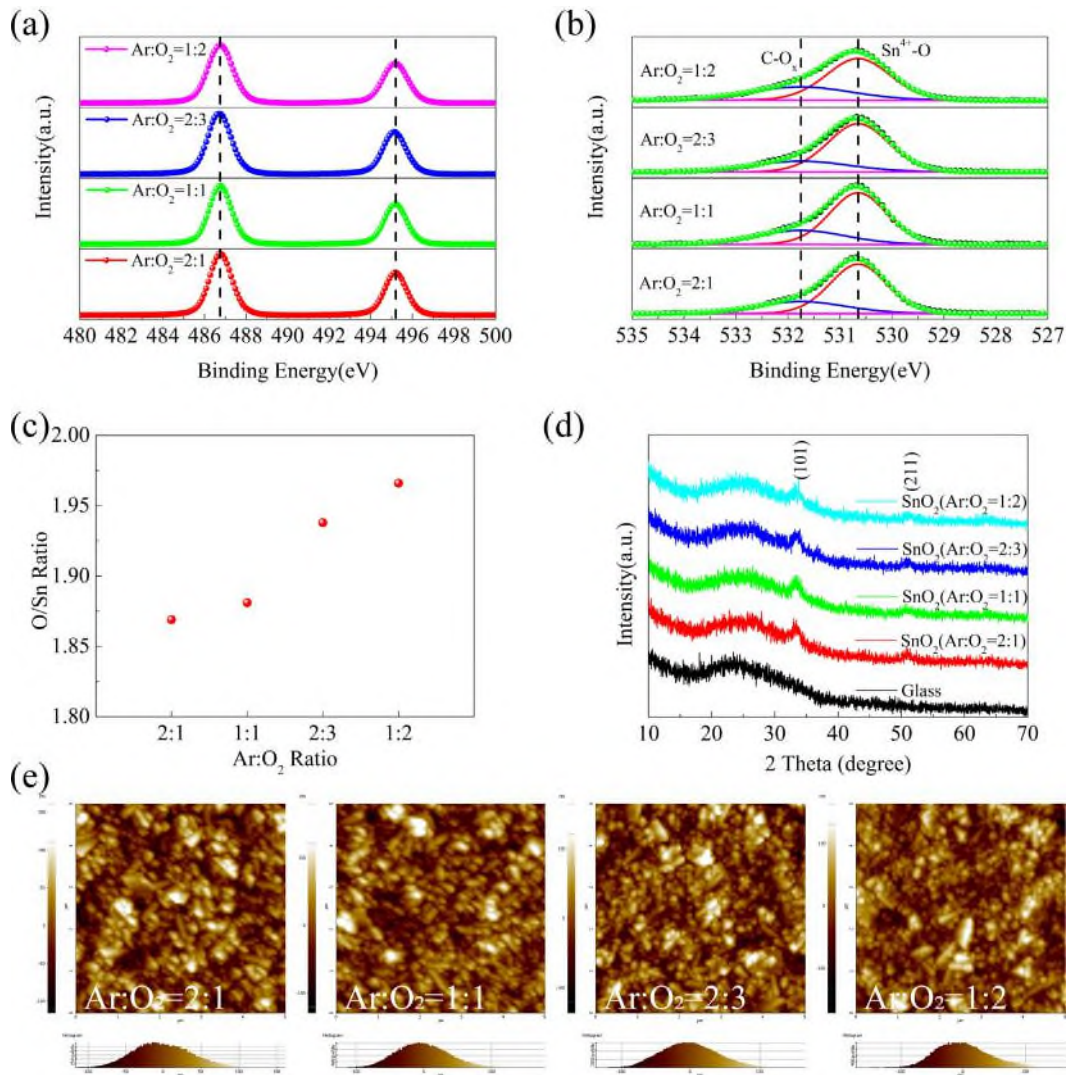


Fig. 2. XPS spectra of (a) Sn 3d, (b) O1s peaks for SnO₂ films, (c) The fitted O/Sn ratio, (d) XRD pattern, (e) AFM image of sputtered SnO₂ films with various Ar/O₂ ratios.

became a bit stronger, demonstrating that the crystallinity of SnO₂ could be influenced by oxygen. Anyway, all the diffraction peaks are not strong enough, revealing a mild crystallization feature. The scanning electron microscope (SEM) images of bare FTO and sputtered SnO₂ film (20 nm) is shown in Fig. S3. The surface morphology of bare FTO is visibly rough with numerous cracks. After sputtering the SnO₂ films in FTO substrate, the cracks are reduced and the sharp edges of FTO crystals turn rounded. The SEM images of SnO₂ film with various Ar/O₂ ratio exhibit similar morphology to bare FTO and show little difference in morphology, indicating that the Ar/O₂ ratio does not affect morphology of sputtered SnO₂.

Atomic force microscope (AFM) is also conducted to further investigate the morphologies and roughness of the sputtered SnO₂ films with different Ar/O₂ ratio. The corresponding AFM images are presented in Fig. 2e. The R_q value of sputtered SnO₂ film are 8.855, 8.964, 10.740 and 14.714 nm for the sputtered SnO₂ film which are processed at different Ar/O₂ ratio (2:1, 1:1, 2:3 and 1:2), respectively. It is obvious that the substrates are completely covered by the sputtered SnO₂ film, which are consistent with the SEM images. With the decrease of Ar/O₂ ratio, the grain size of the sputtered SnO₂ film became larger and tighter. It is no doubt that increasing the oxygen reactive gas could assist in reducing the oxygen vacancy defects and upholding the structure of SnO₂. However, excessive oxygen may introduce interstitial oxygen defects (Zhao et al., 2018b). In addition, the surface roughness

increase from 8.8 nm to 14.7 nm. This may contribute to the reduction of grain boundaries. Moreover, the increased surface roughness is able to increase contact area between perovskite film and ETL, which is beneficial to the charge transfer.

In order to investigate the effect of Ar/O₂ ratio on the device performance, the complete devices were fabricated, based on the sputtered SnO₂ films under various Ar/O₂ ratios (2:1, 1:1, 2:3, 1:2). As shown in Fig. 3b, with decreasing the Ar/O₂ ratio, the device performance is gradually improved the best performing devices are obtained when the Ar/O₂ ratios are decreased to 2:3, showing a high open circuit voltage (V_{oc}) of 1.059 V, a short circuit current density (J_{sc}) of 22.35 mA/cm², and a fill factor (FF) of 73.7%, and a PCE of 17.43%. Further decreasing the Ar/O₂ ratios, however, the performance of PSCs become worse. The detailed photovoltaics parameters are listed in Table 1. The box plots of performance parameters of 16 devices are shown in Fig. 3f, and the statistical table of corresponding parameters is shown in Table S2. The open voltage and fill factor of PSCs change clearly under various Ar/O₂ ratio during the sputtering process. With the increase of oxygen partial pressure during the sputtering process, the vacancies defect in SnO₂ film reduced. Accordingly, the open voltage and fill factor of PSC show a visibly rising tendency. When the introduction of much excessive oxygen gas during the sputtering process, the rising tendency become reverse. It can be concluded that excessive oxygen partial pressure may generate partial interstitial-oxygen in the SnO₂ lattice, which

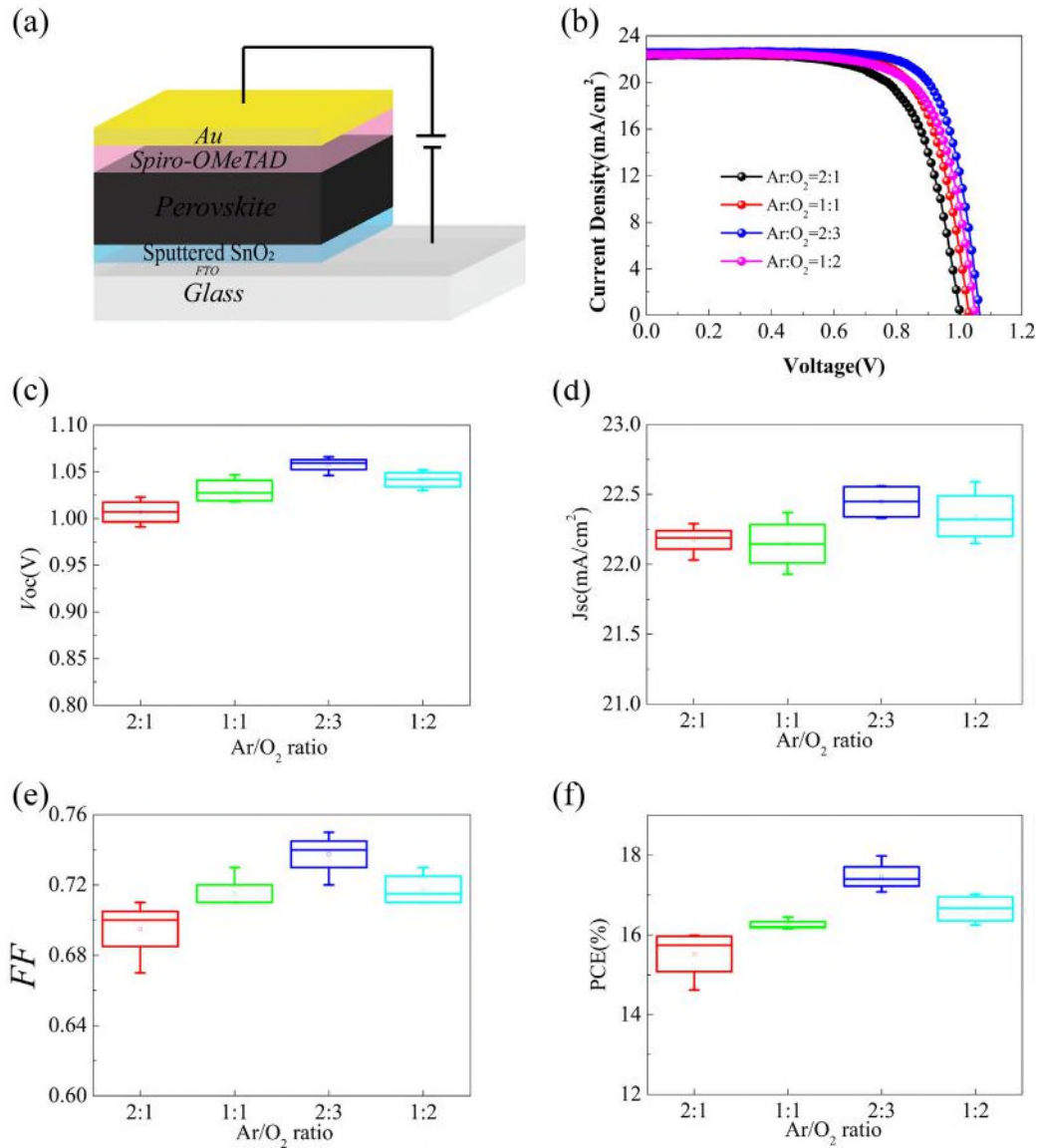


Fig. 3. (a) Schematic illustration of devices structure. (b) J - V curves of PSC based on sputtered SnO₂ film with different Ar/O₂ ratio. (c) V_{oc} , (d) J_{sc} , (e) FF , (f) PCE of statistical 16 devices based on sputtered SnO₂ with different Ar/O₂ ratio.

Table 1
The J - V parameters of the PSCs employing sputtered SnO₂ with different Ar/O₂ ratio.

Ar/O ₂ ratio	V _{oc} (V)	J _{sc} (mA/cm ²)	Fill Factor	Efficiency (%)
2:1	1.002	22.29	0.696	15.54
1:1	1.047	22.2	0.708	16.45
2:3	1.059	22.35	0.737	17.43
1:2	1.052	22.39	0.717	16.88

damage the electrical properties of SnO₂ film (Zhao et al., 2018b).

In addition, the sandwiched structure of FTO/sputtered SnO₂/Au are used to evaluate the conductivity of different SnO₂ film (Bu et al., 2017), as shown in Fig. 4a. The conductivity of SnO₂ film shows a little decrease when the Ar/O₂ ratio decreases to 2:3, indicating lower vacancy defects. However, when further decreasing the Ar/O₂ ratio, it shows a significant decline in conductivity and possible electron extraction.

In order to investigate the defects and charge extraction of these different SnO₂ films, the steady-state photoluminescence (PL) measurements are conducted. The PL spectra of FTO/perovskite and FTO/

the sputtered SnO₂ films with different Ar:O₂/perovskite are shown in Fig. 4b. From the PL spectra of FTO/perovskite, a much stronger PL intensity can be obviously observed, resulting from serious recombination. After inserting SnO₂ layers between FTO and perovskite, the PL spectra show a significant quenching, demonstrating effective electron extraction of sputtered SnO₂ films. When the Ar:O₂ ratio decreases to 2:3, the intensity of PL spectra is weakest, indicating a fast charge transfer. This can be ascribed to the relatively lower oxygen-vacancy defects existed in sputtered SnO₂ film. Similarly, the electron extraction performances at the SnO₂/perovskite interface could be viewed by the time-resolved photoluminescence (TRPL) measurements. As shown in Fig. 4c, it can be clearly found that the lifetime of the perovskite layer can be distinctly reduced when deposited on sputtered SnO₂. Both the PL and TRPL revealed the superior electron extraction of sputter SnO₂ (Ar:O₂ = 2:3) ETL.

As we all know, it is convincing to expose carriers transfer behaviors by electrochemical impedance spectroscopy (EIS) measurements. Fig. 4d shows the Nyquist plots of planar PSCs based on sputtered SnO₂ ETLs measured under AM 1.5 illumination with an applied bias voltage of 1.0 V. There are two different semicircles in the Nyquist plots. The semicircle locate at high frequency ranges corresponds to the internal

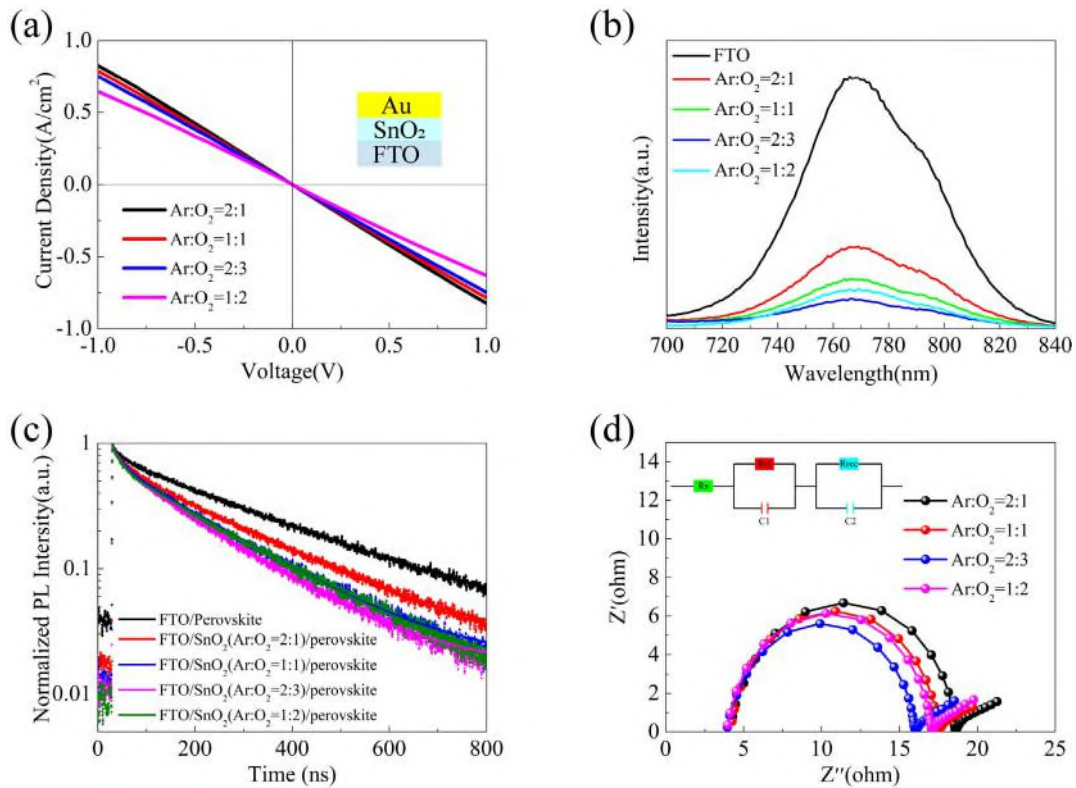


Fig. 4. (a) Conductivity of the sandwiched structure of Au/SnO₂/FTO. (b) Steady-state PL spectra, (c) TRPL spectra of perovskite films contacted with pure FTO and the sputtered SnO₂ films prepared in different Ar/O₂ ratios. (d) EIS plots of PSCs based on different Ar/O₂ ratios.

resistance (R_{ct}) of the devices, and the other semicircle locate at low frequency ranges reflects recombination resistance (R_{rec}) at the SnO₂/perovskite interface, respectively. The fitted results of EIS parameters are shown in Table S3. The fitted R_{ct} of the PSC based on SnO₂ ETL which is sputtered at Ar:O₂ = 2:3 exhibits the smallest semicircle, which indicates fast charge transfer in PSCs. Besides, the PSC based on SnO₂ ETL sputtered at Ar:O₂ = 2:3 showed the largest R_{rec} , demonstrating less recombination occurring at the interface, according to the less defects in the sputtered SnO₂ film.

To further optimize the performance of the PSCs, the devices based on the sputtered SnO₂ films with different thickness are fabricated. Similar to ALD process, the sputter also can obtain compact film in relatively thinner thickness. From Table 2, the SnO₂ film are 10 nm, 20 nm, 30 nm and 40 nm, respectively. The average current density of the device was only 21.8 ± 0.4 mA/cm² and the average FF was 0.68 ± 0.03 when the thickness of the sputtered SnO₂ film is 10 nm, giving rise to the poorer PCE. It may be induced by the slightly incomplete coverage in bulge of FTO. There is a distinct improvement in current density when the thickness of SnO₂ further increased, demonstrating the fully coverage. The same trend can be observed in FF owing to super contact and transfer. However, the reversal in FF occurred when the film thickness exceeds 20 nm. Some literatures reported that increased thickness could increase series resistance in PSC so as to affect charge transfer (Feng et al., 2017; Ma et al., 2017). It also needs longer time to deposit thicker film since the slowly sputter rate. Therefore, the

Table 2
The J - V parameters of PSC based on different thickness of sputtered SnO₂ film.

Thickness (nm)	V_{oc} (V)	J_{sc} (mA/cm ²)	FF	PCE (%)
10	1.05 ± 0.03	21.8 ± 0.4	0.68 ± 0.03	15.8 ± 0.8
20	1.05 ± 0.02	22.3 ± 0.4	0.74 ± 0.02	17.8 ± 0.4
30	1.02 ± 0.03	22.3 ± 0.3	0.70 ± 0.03	15.9 ± 0.9
40	0.93 ± 0.04	22.1 ± 0.4	0.68 ± 0.03	14.1 ± 0.6

best thickness of sputtered SnO₂ ETL is controlled at 20 nm.

Inspired by annealing treatment of SnO₂ film prepared by solution-based method (Li et al., 2018a; Liu et al., 2018), we also conduct post-annealing experiments for sputtered SnO₂ film, expecting to acquire higher efficiency. Fig. S5 showed the J - V curves of PSC based on RF sputtering SnO₂ with various anneal temperature. Obviously, the devices performance goes worse as the improvement of annealing temperature. We also fabricate 16 devices based on various post-annealing temperature to acquire statistical tendency, shown in Table S4. As the annealing temperature increase, the FF and V_{oc} of devices exhibits a visible downward trend. The oxygen vacancy, O/Sn ratio, and conductivity of SnO₂ film may get changed during the post anneal process (Ke et al., 2015). Besides, our devices based on room-temperature sputtered SnO₂ film exhibits mild hysteresis without interface process. One of the solution for the hysteresis is to adjust the recipes of per-ovskite materials (Bu et al., 2017). To reduce the cost of fabrication maximally, and improve devices performance at the same time, we employ $K_{0.03}Cs_{0.05}FA_{0.85}MA_{0.15}Pb(I_{0.85}Br_{0.15})_3$ perovskite material according to our previous reports (Bu et al., 2017). The corresponding results are shown in Fig. S4. The hysteresis can be eliminated by adding K⁺ into perovskite solution and we acquired an efficiency of 16.42% under reverse scan and an efficiency 16.38% under forward scan.

In order to evaluate the reproducibility of PSCs based on room-temperature sputtered SnO₂ film, 30 devices were fabricated at optimized Ar/O₂ ratio and thickness. The histogram of PCE is shown in Fig. 5a. It can be concluded that sputtered SnO₂ had excellent reproducibility resulting from the tiny undulation of the photovoltaic performance. In spite of no any other interface optimization, the average of those devices using sputtered SnO₂ ETL is 17.8% and the best performance (Fig. 5b) of PSC display the champion PCE of 18.20%, harvesting a J_{sc} of 22.45 mA/cm², a V_{oc} of 1.056 V, and a FF of 0.76. The corresponding external quantum efficiency (EQE) spectrum of the best device is shown in Fig. 5c, exhibiting a strong and extensive light response over the whole UV visible light wavelength range. The

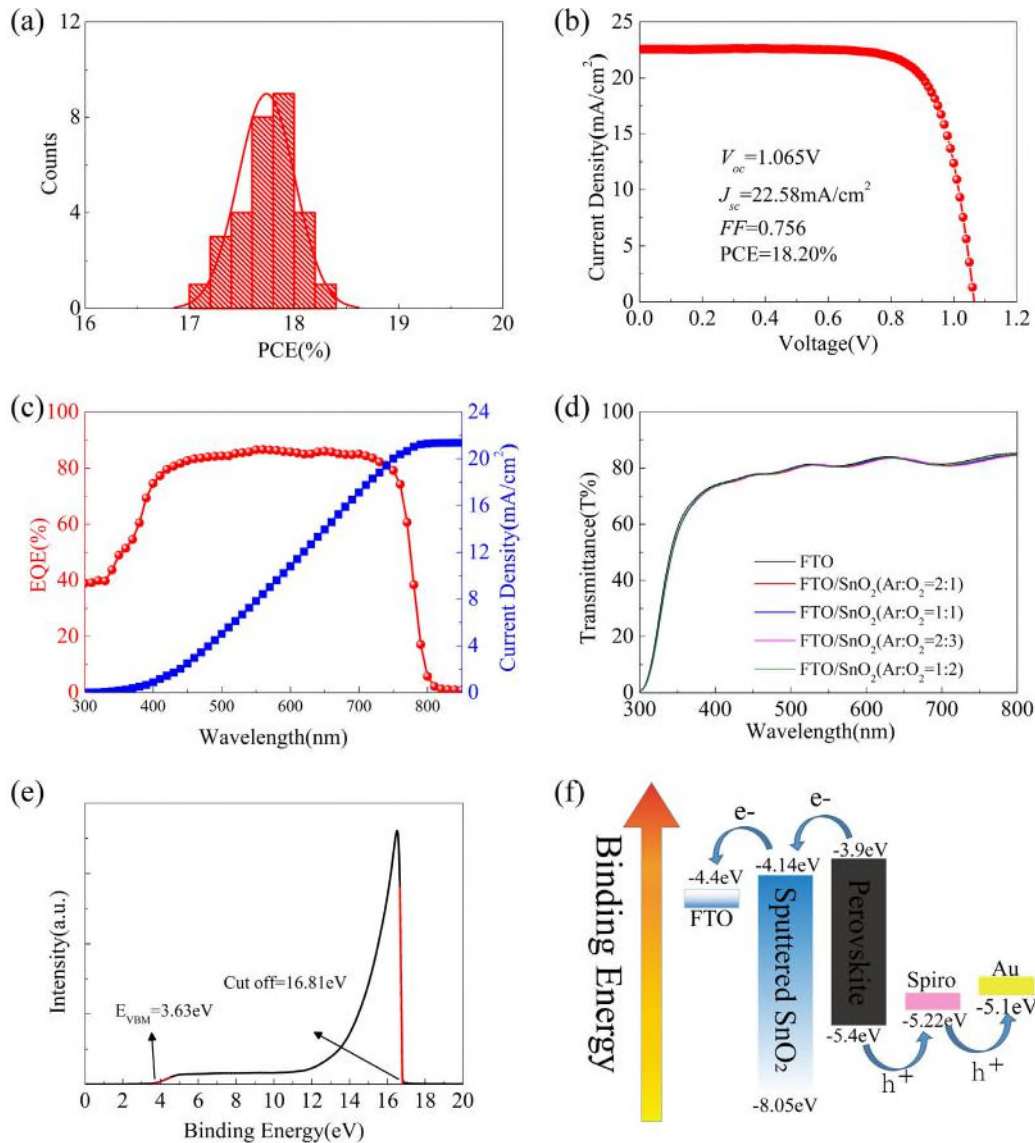


Fig 5. (a) A histogram of PCEs for 30 devices based on sputtered SnO₂ ETL. (b) the J - V curves of champion efficiency, (c) The corresponding EQE spectrum of PSC based on sputtered SnO₂ ETL. (d) Transmittance spectrum of sputtered SnO₂. (e) UPS spectrum of sputtered SnO₂ film (Ar:O₂ = 2:3). (f) Energy band schematic view of the device.

integrated current density is figured out to be 21.4 mA/cm² by the fitting analysis of EQE curve, in accord with the values obtained from the J - V measurement.

The transmittance spectrum of sputtered SnO₂ is shown in Fig. 5d, indicates high transmittance in the visible region and slight antire-flection effect in some wavelength range, which can minimize optical loss and enhances the light absorption of perovskite layer. The optical energy gap (E_g) of sputtered SnO₂ under various Ar/O₂ ratio are calculated as 3.91 eV from transmittance spectra (Fig. S6), it can be conclude that the Ar/O₂ ratio have little effect on optical energy gap of sputtered SnO₂. We have characterized the band structure of sputtered SnO₂ (Ar:O₂ = 2:3) with ultraviolet photoelectron spectroscopy (UPS). As shown in Fig. 5e, the work function (\bar{W}_s) and valance band maximum (VBM) of sputtered SnO₂ are -4.4 eV and -3.63 eV, respectively. The conduction band (E_c) of sputtered SnO₂ is calculated as -4.14 eV from the equation: $E_c = \bar{W}_s + VBM - E_g$ based on the semiconductor band structure (Jiang et al., 2016). Comparing to the perovskite material (FA_{0.88}MA_{0.15}Pb(I_{0.88}Br_{0.15})₃), slightly deeper conduction band of sputtered SnO₂ could ensure charge transfer and much lower valence band is beneficial to block holes from the perovskite layer. The matched

band alignment confirms that sputtered SnO₂ film is well suitable to be used in PSC.

For better use the uniformity and reproducibility of RF sputtered SnO₂ film, we sputtered 5×6 cm² films for the ETL of PSC. The sub-module of PSC with an aperture area of 16.07 cm² is prepared using sputtered SnO₂ film. The photograph of a perovskite sub-module is shown in Fig. 6a. The champion sub-module comprise 6 series connected cells yield a PCE of 14.71%, a V_{oc} of 6.082 V, a J_{sc} of 3.54 mA/cm² and a FF of 0.683 under 1 Sun AM 1.5G illumination, as shown in Fig. 6b. All of above results indicate a prominent prospect of sputter SnO₂ ETL for future industry application of PSC.

4. Conclusions

In summary, we fabricated efficient and large-area perovskite solar modules with sputtered SnO₂ ETLs. By adjusting the Ar/O₂ gas ratio in the RF sputtering process, we found O/Sn ratio in SnO₂ film plays a crucial role in high performance of PSC. Characterizations revealed that appropriate conductivity, less defect density and fast charge transportation of optimized SnO₂ composition have all made contributions to

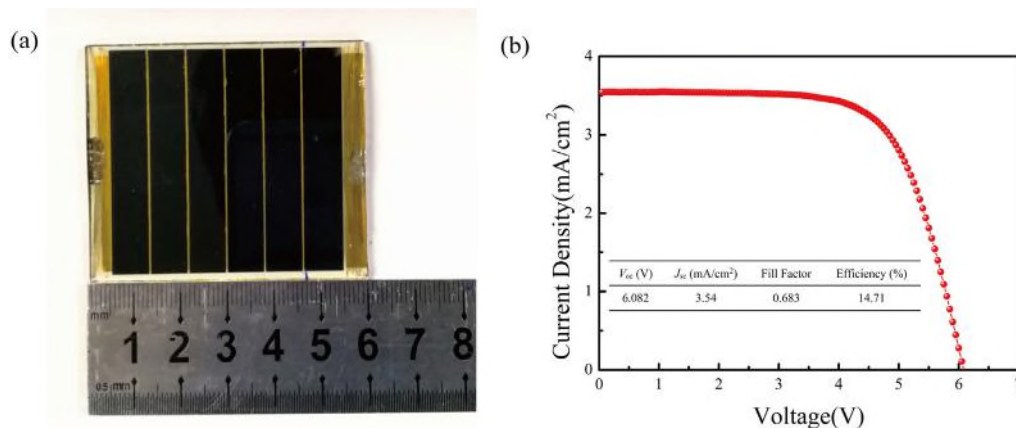


Fig. 6. (a) The photograph of perovskite sub-module. (b) J - V curve of perovskite sub-module.

improvement of device performance. Further optimized thickness and annealing temperature, we achieved an efficiency of 18.20% in small area PSC. Moreover, a high efficiency sub-modules (5×6 cm) up to 14.71% with aperture area of 16.07 cm^2 have been fabricated, demonstrating great promising for large scale industry application of sputter SnO_2 .

Acknowledgements

This work is financially supported by National Natural Science Foundation of China (NSFC 51672202, 51702243), Hubei Provincial Natural Science Foundation of China (2016CFB464), the Technological Innovation Key Project of Hubei Province (2016AAA041), National College Students Innovation and Entrepreneurship Training Program (20181049701028). JZ thanks the support the “Chutian Scholar Program” of Hubei Province, China.

References

Albrecht, S., Saliba, M., Correa Baena, J.P., Lang, F., Kegelmann, L., Mews, M., Steier, L., Abate, A., Rappich, J., Korte, L., Schlattmann, R., Nazeeruddin, M.K., Hagfeldt, A., Grätzel, M., Rech, B., 2016. Monolithic perovskite/silicon-heterojunction tandem solar cells processed at low temperature. *Energy Environ. Sci.* 9, 81–88.

Ali, F., Pham, N.D., Bradford, H.J., Khoshirsat, N., Ostrikov, K., Bell, J.M., Wang, H., Tesfamichael, T., 2018. Tuning the amount of oxygen vacancies in sputter-deposited SnO_x films for enhancing the performance of perovskite solar cells. *ChemSusChem* 11, 3096–3103.

Anaraki, E.H., Kermanpur, A., Steier, L., Domanski, K., Matsui, T., Tress, W., Saliba, M., Abate, A., Grätzel, M., Hagfeldt, A., Correa-Baena, J.-P., 2016. Highly efficient and stable planar perovskite solar cells by solution-processed tin oxide. *Energy Environ. Sci.* 9, 3128–3134.

Aydin, E., Troughton, J., De Bastiani, M., Ugur, E., Sajjad, M., Alzahrani, A., Neophytou, M., Schwingenschlögler, U., Laquai, F., Baran, D., De Wolf, S., 2018. Room-temperature-sputtered nanocrystalline nickel oxide as hole transport layer for p-i-n perovskite solar cells. *ACS Appl. Energy Mater.* 1, 6227–6233.

Bu, T., Li, J., Zheng, F., Chen, W., Wen, X., Ku, Z., Peng, Y., Zhong, J., Cheng, Y.B., Huang, F., 2018. Universal passivation strategy to slot-die printed SnO_2 for hysteresis-free efficient flexible perovskite solar module. *Nat. Commun.* 9, 4609.

Bu, T., Liu, X., Zhou, Y., Yi, J., Huang, X., Luo, L., Xiao, J., Ku, Z., Peng, Y., Huang, F., Cheng, Y.-B., Zhong, J., 2017. A novel quadruple-cation absorber for universal hysteresis elimination for high efficiency and stable perovskite solar cells. *Energy Environ. Sci.* 10, 2509–2515.

Bu, T., Wen, M., Zou, H., Wu, J., Zhou, P., Li, W., Ku, Z., Peng, Y., Li, Q., Huang, F., Cheng, Y.-B., Zhong, J., 2016. Humidity controlled sol-gel Zr/TiO_2 with optimized band alignment for efficient planar perovskite solar cells. *Sol. Energy* 139, 290–296.

Bush, K.A., Manzoor, S., Frohna, K., Yu, Z.J., Raiford, J.A., Palmstrom, A.F., Wang, H.-P., Prasanna, R., Bent, S.F., Holman, Z.C., McGehee, M.D., 2018. Minimizing current and voltage losses to reach 25% efficient monolithic two-terminal perovskite-silicon tandem solar cells. *ACS Energy Lett.* 3, 2173–2180.

Chen, Y., Meng, Q., Zhang, L., Han, C., Gao, H., Zhang, Y., Yan, H., 2019. SnO_2 -based electron transporting layer materials for perovskite solar cells: a review of recent progress. *J. Energy Chem.* 35, 144–167.

Chen, Z., Yang, G., Zheng, X., Lei, H., Chen, C., Ma, J., Wang, H., Fang, G., 2017. Bulk heterojunction perovskite solar cells based on room temperature deposited hole-blocking layer: suppressed hysteresis and flexible photovoltaic application. *J. Power Sour.* 351, 123–129.

Correa-Baena, J.-P., Saliba, M., Buonassisi, T., Grätzel, M., Abate, A., Tress, W., Hagfeldt, A., 2017. Promises and challenges of perovskite solar cells. *Science* 358, 739–744.

Correa Baena, J.P., Steier, L., Tress, W., Saliba, M., Neutzner, S., Matsui, T., Giordano, F., Jacobsson, T.J., Srimath Kandada, A.R., Zakeeruddin, S.M., Petrozza, A., Abate, A., Nazeeruddin, M.K., Grätzel, M., Hagfeldt, A., 2015. Highly efficient planar perovskite solar cells through band alignment engineering. *Energy Environ. Sci.* 8, 2928–2934.

Feng, J., Yang, Z., Yang, D., Ren, X., Zhu, X., Jin, Z., Zi, W., Wei, Q., Liu, S., 2017. E-beam evaporated Nb_2O_5 as an effective electron transport layer for large flexible perovskite solar cells. *Nano Energy* 36, 1–8.

Feng, J., Zhu, X., Yang, Z., Zhang, X., Niu, J., Wang, Z., Zuo, S., Priya, S., Liu, S., Yang, D., 2018. record efficiency stable flexible perovskite solar cell using effective additive assistant strategy. *Adv. Mater.* 30, 1801418.

Guo, X., Dong, H., Li, W., Li, N., Wang, L., 2015. Multifunctional MgO layer in perovskite solar cells. *ChemPhysChem* 16, 1727–1732.

Guo, Y., Jiang, J., Zuo, S., Shi, F., Tao, J., Hu, Z., Hu, X., Hu, G., Yang, P., Chu, J., 2018. RF sputtered CdS films as independent or buffered electron transport layer for efficient planar perovskite solar cell. *Sol. Energy Mater. Sol. Cells* 178, 186–192.

Halvani Anaraki, E., Kermanpur, A., Mayer, M.T., Steier, L., Ahmed, T., Turren-Cruz, S.-H., Seo, J., Luo, J., Zakeeruddin, S.M., Tress, W.R., Edvinsson, T., Grätzel, M., Hagfeldt, A., Correa-Baena, J.-P., 2018. Low-temperature Nb -doped SnO_2 electron-selective contact yields over 20% efficiency in planar perovskite solar cells. *ACS Energy Lett.* 3, 773–778.

Huang, A., Lei, L., Zhu, J., Yu, Y., Liu, Y., Yang, S., Bao, S., Cao, X., Jin, P., 2017. Achieving high current density of perovskite solar cells by modulating the dominated facets of room-temperature DC magnetron sputtered TiO_2 electron extraction layer. *ACS Appl. Mater. Interfaces* 9, 2016–2022.

Huang, M.-C., Chang, W.-S., Lin, J.-C., Chang, Y.-H., Wu, C.-C., 2015. Magnetron sputtering process of carbon-doped $\alpha\text{-Fe}_2\text{O}_3$ thin films for photoelectrochemical water splitting. *J. Alloy Compd.* 636, 176–182.

Jeon, N.J., Na, H., Jung, E.H., Yang, T.-Y., Lee, Y.G., Kim, G., Shin, H.-W., Il Seok, S., Lee, J., Seo, J., 2018. A fluorene-terminated hole-transporting material for highly efficient and stable perovskite solar cells. *Nat. Energy* 3, 682–689.

Jiang, Q., Zhang, L., Wang, H., Yang, X., Meng, J., Liu, H., Yin, Z., Wu, J., Zhang, X., You, J., 2016. Enhanced electron extraction using SnO_2 for high-efficiency planar-structure $\text{HC}(\text{NH}_2)_2\text{PbI}_3$ -based perovskite solar cells. *Nat. Energy* 2.

Ke, W., Zhao, D., Cimaroli, A.J., Grice, C.R., Qin, P., Liu, Q., Xiong, L., Yan, Y., Fang, G., 2015. Effects of annealing temperature of tin oxide electron selective layers on the performance of perovskite solar cells. *J. Mater. Chem. A* 3, 24163–24168.

Kogo, A., Sanehira, Y., Numata, Y., Ikegami, M., Miyasaka, T., 2018. Amorphous metal oxide blocking layers for highly efficient low-temperature brookite TiO_2 -based perovskite solar cells. *ACS Appl. Mater. Interfaces* 10, 2224–2229.

Lee, D.H., Song, D., Kang, Y.S., Park, W.I., 2015. Three-dimensional monolayer graphene and TiO_2 hybrid architectures for high-efficiency electrochemical photovoltaic cells. *J. Phys. Chem. C* 119, 6880–6885.

Leijtens, T., Bush, K.A., Prasanna, R., McGehee, M.D., 2018. Opportunities and challenges for tandem solar cells using metal halide perovskite semiconductors. *Nat. Energy* 3, 828–838.

Li, J., Bu, T., Liu, Y., Zhou, J., Shi, J., Ku, Z., Peng, Y., Zhong, J., Cheng, Y.B., Huang, F., 2018a. Enhanced crystallinity of low-temperature solution-processed SnO_2 for highly reproducible planar perovskite solar cells. *ChemSusChem* 11, 2898–2903.

Li, Z., Klein, T.R., Kim, D.H., Yang, M., Berry, J.J., van Hest, M.F.A.M., Zhu, K., 2018b. Scalable fabrication of perovskite solar cells. *Nat. Rev. Mater.* 3, 18017.

Liu, X., Bu, T., Li, J., He, J., Li, T., Zhang, J., Li, W., Ku, Z., Peng, Y., Huang, F., Cheng, Y.-B., Zhong, J., 2018. Stacking n-type layers: effective route towards stable, efficient and hysteresis-free planar perovskite solar cells. *Nano Energy* 44, 34–42.

- Ma, J., Zheng, X., Lei, H., Ke, W., Chen, C., Chen, Z., Yang, G., Fang, G., 2017. Highly efficient and stable planar perovskite solar cells with large-scale manufacture of E-beam evaporated SnO₂ toward commercialization. *Solar RRL* 1, 1700118.
- Petrović, M., Ye, T., Vijila, C., Ramakrishna, S., 2017. Influence of charge transport and defects on the performance of planar and mesostructured perovskite solar cells. *Adv. Energy Mater.* 7, 1602610.
- Qiu, L., Liu, Z., Ono, L.K., Jiang, Y., Son, D.-Y., Hawash, Z., He, S., Qi, Y., 2018. Scalable fabrication of stable high efficiency perovskite solar cells and modules utilizing room temperature sputtered SnO₂ electron transport layer. *Adv. Funct. Mater.* 1806779.
- Roose, B., Gödel, K.C., Pathak, S., Sadhanala, A., Baena, J.P.C., Wilts, B.D., Snaith, H.J., Wiesner, U., Grätzel, M., Steiner, U., Abate, A., 2016. Enhanced efficiency and stability of perovskite solar cells through Nd-doping of mesostructured TiO₂. *Adv. Energy Mater.* 6, 1501868.
- Silva Filho, J.M.C.d., Ermakov, V.A., Marques, F.C., 2018. Perovskite thin film synthesised from sputtered lead sulphide. *Sci. Rep.* 8, 1563.
- Tao, H., Ma, Z., Yang, G., Wang, H., Long, H., Zhao, H., Qin, P., Fang, G., 2018. Room-temperature processed tin oxide thin film as effective hole blocking layer for planar perovskite solar cells. *Appl. Surf. Sci.* 434, 1336–1343.
- Wang, C., Zhao, D., Grice, C.R., Liao, W., Yu, Y., Cimaroli, A., Shrestha, N., Roland, P.J., Chen, J., Yu, Z., Liu, P., Cheng, N., Ellingson, R.J., Zhao, X., Yan, Y., 2016. Low-temperature plasma-enhanced atomic layer deposition of tin oxide electron selective layers for highly efficient planar perovskite solar cells. *J. Mater. Chem. A* 4, 12080–12087.
- Xie, M., Lu, H., Zhang, L., Wang, J., Luo, Q., Lin, J., Ba, L., Liu, H., Shen, W., Shi, L., Ma, C.-Q., 2018. Fully solution-processed semi-transparent perovskite solar cells with ink-jet printed silver nanowires top electrode. *Solar RRL* 2, 1700184.
- Xue, Q., Xia, R., Brabec, C.J., Yip, H.-L., 2018. Recent advances in semi-transparent polymer and perovskite solar cells for power generating window applications. *Energy Environ. Sci.* 11, 1688–1709.
- Yang, D., Yang, R., Wang, K., Wu, C., Zhu, X., Feng, J., Ren, X., Fang, G., Priya, S., Liu, S., 2018a. High efficiency planar-type perovskite solar cells with negligible hysteresis using EDTA-complexed SnO₂. *Nat. Commun.* 9, 3239.
- Yang, G., Chen, C., Yao, F., Chen, Z., Zhang, Q., Zheng, X., Ma, J., Lei, H., Qin, P., Xiong, L., Ke, W., Li, G., Yan, Y., Fang, G., 2018b. Effective carrier-concentration tuning of SnO₂ quantum dot electron-selective layers for high-performance planar perovskite solar cells. *Adv. Mater.* 30, e1706023.
- Yin, X., Xu, Z., Guo, Y., Xu, P., He, M., 2016. Ternary oxides in the TiO₂-ZnO system as efficient electron-transport layers for perovskite solar cells with efficiency over 15%. *ACS Appl. Mater. Interfaces* 8, 29580–29587.
- Zhang, F., Ma, W., Guo, H., Zhao, Y., Shan, X., Jin, K., Tian, H., Zhao, Q., Yu, D., Lu, X., Lu, G., Meng, S., 2016. Interfacial oxygen vacancies as a potential cause of hysteresis in perovskite solar cells. *Chem. Mater.* 28, 802–812.
- Zhang, Y., Wu, Z., Li, P., Ono, L.K., Qi, Y., Zhou, J., Shen, H., Surya, C., Zheng, Z., 2018. Fully solution-processed TCO-Free semitransparent perovskite solar cells for tandem and flexible applications. *Adv. Energy Mater.* 8, 1701569.
- Zhao, D., Wang, C., Song, Z., Yu, Y., Chen, C., Zhao, X., Zhu, K., Yan, Y., 2018a. Four-terminal all-perovskite tandem solar cells achieving power conversion efficiencies exceeding 23%. *ACS Energy Lett.* 3, 305–306.
- Zhao, W., Wang, K., Li, H., Yang, Z., Liu, Z., Sun, J., Wang, D., Liu, S., 2018b. Stoichiometry control of sputtered zinc oxide films by adjusting Ar/O₂ gas ratios as electron transport layers for efficient planar perovskite solar cells. *Sol. Energy Mater. Sol. Cells* 178, 200–207.